

ML-Index Methods

David Moreau

October 17, 2024

My understand of reading through powder diffraction indexing methods papers is that existing algorithms work really well on good data. The SVD-Index index algorithm showed 100% accuracy in their paper with peak lists generated with random unit cells. The biggest issue is the generalization of these algorithms to real experimental data, especially low quality data. So the benchmark for this project is near perfect results on calculated data, or demonstrating superior generality to experimental data. The future development of this project will follow the following development cycle:

1. Demonstrate that this algorithm works well on ideal data by pushing the monoclinic and triclinic indexing rates into the 90's on the current dataset calculated from CCDC / COD entries.
2. Determine appropriate levels of experimental error through characterize experimental peak lists from our smSFX data.
3. Start generalization by regenerating datasets with experimental error and testing the performance. The experimental error will be incorporated in the following order: 1) missing peaks at a realistic rate, 2) error in peak positions, 3) contaminant peaks. Eventually a zero error will need to be included, but is a low priority.

Text in italics is commentary. For example, my hunches, opinions, acknowledgments of errors and bugs in the code, or features and approaches I would like to take, and features that are implemented but not used. Normal case text describes currently implemented methods.

| Bravais Lattice | Indexing Rate |
|-----------------|---------------|
| aP | 61 - 84% |
| cF | 99.5% |
| cI | 100.0% |
| cP | 99.7% |
| hP | 99.5% |
| hR | 92 - 99.4% |
| mC | 81 - 92% |
| mP | 85% |
| oC | 98.5% |
| oF | 99.0% |
| oI | 99.0% |
| oP | 99.5% |
| tI | 99.0% |
| tP | 99.5% |

Table 1: Current indexing rates. This is the ability to index a set of 20 diffraction peaks (10 for cubic). If a range is given, the lower number is the rate for finding the exact or symmetry equivalent unit cell. The higher number is the rate for providing a unit cell that can explain the diffraction pattern to within round-off error.

1 Introduction

Powder diffraction indexing is the process of using a 1-dimensional projection of the 3-dimensional diffraction to infer the symmetries that exist within a material. This is a problem as old as crystallography (Runge 1917 *Additional citations - Andrews & Bernstein cite these*) and has been the subject of many analytical efforts. Current trends in machine learning and artificial intelligence have produced new knowledge and tools for data-driven analytics. This project merges recent advancements in analytical methods with knowledge from existing indexing algorithms to produce a new approach to powder diffraction indexing.

This algorithm is developed with general use in mind, but the foremost use case is the small molecule serial crystallography community (Schriber, et. al. 2022). This software is developed as an open-source Python program, in line with the Computational Crystallography Initiative (CITE). Serial femtosecond crystallography data analysis is performed exclusively on super-computers and computational clusters. ML-Index is developed specifically for mass-distributed computing.

1.1 Inspirational Quotes

- de Wolff 1957: The 'indexing problem' is essentially a puzzle: it cannot be stated in rigorous terms, or be solved in a general way by clear-cut methods, because of the unpredictable distribution of unobserved lines in a powder pattern. It would be quite an easy puzzle if errors of measurement did not exist. This added inconvenience, however, is enough to raise some doubt as to whether the determination of the unit cell of an arbitrary polycrystalline phase is possible in, say, an average of half a day's work or less.

Le Bail (2004) provides some quotes:

- 'Indexing is more an art than a science,'
- 'It is entirely the users responsibility to decide whether any of the suggested unit cells is the correct cell' (ITO manual)
- 'Powder indexing works beautifully on good data, but with poor data it will usually not work at all' (Shirley, 1980)
- 'DICVOL proposes solutions, the user disposes of them' (DICVOL manual)
- Users now want solutions fast, without thinking too much, ignoring that 'part of the beauty of structure determination by powder diffraction does consist in its complexity, i.e., in the lack of complete automatism as well as in the necessity of a careful and sagacious human interpretation of the experimental data,' (anonymous reviewer)

1.2 Powder diffraction indexing

Diffraction is produced in 3-dimensional spherical coordinates - reciprocal space. In the powder diffraction method, the 3d diffraction pattern is recorded in the radial dimension, the distance of the measured diffraction from the center of the spherical coordinate system. The recorded pattern is a series of peaks with the location of the peaks representing the spacing of Miller planes through the crystal's unit cell. In the indexing problem, the objective is to determine the unit cell level symmetries of the crystal that produced this pattern. When the diffraction is in coordinates of $q = \frac{2 \sin(\theta)}{\lambda}$, where θ is the diffraction angle and λ is the wavelength, the crystal's unit cell can be related to the observed peak locations with through the general equation:

$$q_{hkl}^2 = \frac{1}{V} (S_{hh}h^2 + S_{kk}k^2 + S_{ll}l^2 + S_{hk}hk + S_{hl}hl + S_{kl}kl), \quad (1)$$

$$\begin{aligned} S_{hh} &= b^2c^2 \sin^2(\alpha), \\ S_{kk} &= a^2c^2 \sin^2(\beta), \\ S_{ll} &= a^2b^2 \sin^2(\gamma), \\ S_{hk} &= abc^2 [\cos(\alpha)\cos(\beta) - \cos(\gamma)], \\ S_{hl} &= a^2bc [\cos(\beta)\cos(\gamma) - \cos(\alpha)], \\ S_{kl} &= ab^2c [\cos(\alpha)\cos(\gamma) - \cos(\beta)], \\ V(\text{Volume}) &= abc\sqrt{1 - \cos^2(\alpha) - \cos^2(\beta) - \cos^2(\gamma) + 2\cos(\alpha)\cos(\beta)\cos(\gamma)}. \end{aligned}$$

This general equation assumes no constraints among the crystal lattice lengths, a, b, c , and angles, α, β, γ . It is simplified by the lattice parameters constraints defining the seven lattice systems,

triclinic : $a \neq b \neq c, \alpha \neq \beta \neq \gamma \neq 90^\circ$

cubic : $a = b = c, \alpha = \beta = \gamma = 90^\circ$

$$q_{hkl}^2 = \frac{h^2 + k^2 + l^2}{a^2}, \quad (2)$$

tetragonal : $a = b \neq c, \alpha = \beta = \gamma = 90^\circ$

$$q_{hkl}^2 = \frac{h^2 + k^2}{a^2} + \frac{l^2}{c^2} \quad (3)$$

hexagonal : $a = b \neq c, \alpha = \beta = 90^\circ, \gamma = 120^\circ$

$$q_{hkl}^2 = \frac{4}{3} \frac{h^2 + hk + k^2}{a^2} + \frac{l^2}{c^2} \quad (4)$$

rhombohedral : $a = b = c$, $\alpha = \beta = \gamma \neq 90^\circ$

$$q_{hkl}^2 = \frac{(h^2 + k^2 + l^2) \sin^2(\alpha) + 2(hk + kl + hl)(\cos^2(\alpha) - \cos(\alpha))}{a^2(1 - 3\cos^2(\alpha) + 2\cos^3(\alpha))} \quad (5)$$

orthorhombic : $a \neq b \neq c$, $\alpha = \beta = \gamma = 90^\circ$

$$q_{hkl}^2 = \frac{h^2}{a^2} + \frac{k^2}{b^2} + \frac{l^2}{c^2} \quad (6)$$

monoclinic : $a \neq b \neq c$, $\alpha = \gamma = 90^\circ$, $\beta \neq 90^\circ$

$$q_{hkl}^2 = \frac{h^2}{a^2 \sin^2(\beta)} + \frac{k^2}{b^2} + \frac{l^2}{c^2 \sin^2(\beta)} - \frac{2hl \cos(\beta)}{ac \sin^2(\beta)} \quad (7)$$

The triclinic lattice system imposes no unit cell parameter constraints and is known as the triclinic lattice system. The general case gives the peak spacing formula.

These equations can be rewritten in the reciprocal space unit cell parameters, a^* , b^* , c^* , α^* , β^* , γ^* , which are related to the real-space unit cell parameters through the inverse of the metric tensor,

$$S = \begin{pmatrix} a^2 & ab \cos(\gamma) & ac \cos(\beta) \\ ab \cos(\gamma) & b^2 & bc \cos(\alpha) \\ ac \cos(\beta) & bc \cos(\alpha) & c^2 \end{pmatrix} = \begin{pmatrix} a^{*2} & a^{*b^*} \cos(\gamma^*) & a^{*c^*} \cos(\beta^*) \\ a^{*b^*} \cos(\gamma^*) & b^{*2} & b^{*c^*} \cos(\alpha^*) \\ a^{*c^*} \cos(\beta^*) & b^{*c^*} \cos(\alpha^*) & c^{*2} \end{pmatrix}^{-1} \quad (8)$$

Eq. 1-7 can be rewritten using reciprocal space unit cells,

triclinic : $a^* \neq b^* \neq c^*$, $\alpha^* \neq \beta^* \neq \gamma^* \neq 90^\circ$

$$q_{hkl}^2 = a^{*2}h^2 + b^{*2}k^2 + c^{*2}l^2 + 2a^{*b^*} \cos(\gamma^*)hk + 2a^{*c^*} \cos(\beta^*)hl + 2b^{*c^*} \cos(\alpha^*)kl \quad (9)$$

cubic : $a^* = b^* = c^*$, $\alpha^* = \beta^* = \gamma^* = 90^\circ$

$$q_{hkl}^2 = (h^2 + k^2 + l^2) a^{*2} \quad (10)$$

tetragonal : $a^* = b^* \neq c^*$, $\alpha^* = \beta^* = \gamma^* = 90^\circ$

$$q_{hkl}^2 = (h^2 + k^2) a^{*2} + l^2 c^{*2} \quad (11)$$

hexagonal : $a^* = b^* \neq c^*$, $\alpha^* = \beta^* = 90^\circ$, $\gamma^* = 60^\circ$

$$q_{hkl}^2 = (h^2 + hk + k^2) a^{*2} + l^2 c^{*2} \quad (12)$$

rhombohedral : $a^* = b^* = c^*$, $\alpha^* = \beta^* = \gamma^* \neq 90^\circ$

$$q_{hkl}^2 = (h^2 + k^2 + l^2) a^{*2} + 2(hk + kl + hl) a^{*2} \cos(\alpha^*) \quad (13)$$

orthorhombic : $a^* \neq b^* \neq c^*$, $\alpha^* = \beta^* = \gamma^* = 90^\circ$

$$q_{hkl}^2 = h^2 a^{*2} + k^2 b^{*2} + l^2 c^{*2} \quad (14)$$

monoclinic : $a^* \neq b^* \neq c^*$, $\alpha^* = \gamma^* = 90^\circ$, $\beta^* \neq 90^\circ$

$$q_{hkl}^2 = h^2 a^{*2} + k^2 b^{*2} + l^2 c^{*2} + 2a^{*c^*} \cos(\beta^*)hl \quad (15)$$

Eq. 8-15 can be rewritten as a linear function of reciprocal unit cell parameters and Miller indices,

$$q_{hkl}^2 = x_{hh}h^2 + x_{kk}k^2 + x_{ll}l^2 + x_{hk}hk + x_{hl}hl + x_{kl}kl \quad (16)$$

$$\begin{aligned} x_{hh} &= a^{*2}, \\ x_{kk} &= b^{*2}, \\ x_{ll} &= c^{*2}, \\ x_{hk} &= 2a^{*b^*} \cos(\gamma^*), \\ x_{hl} &= 2a^{*c^*} \cos(\beta^*), \\ x_{kl} &= 2b^{*c^*} \cos(\alpha^*). \end{aligned}$$

$$\bar{q}_{hkl}^2 = H \cdot \vec{x}_{nn}. \quad (17)$$

In the linear model, Eq. 17, the observed peak positions are within the vector \bar{q}_{hkl}^2 , information about the Miller indices is contained in matrix H , and information about the unit cell is contained in vector \vec{x}_{nn} . The implication of this linear model is that given a set of observed peak positions and a hypothesis for Miller indices or unit cell, linear methods can be employed to analytically determine the complementary information.

1.2.1 Difficulties with perfect data

In practice, obtaining the solution to the inverse problem of Eq. 1-7 is hindered by numerous obstacles which can be separated into two types; those that will occur with "perfect data" and those that occur due to measurement errors.

Existing powder diffraction indexing methods generally perform well on high quality data and the primary suggestion for increasing the odds of a solution is to obtain better data (Bergmann 2004, Shirley 2003). In the case of perfect data, such as powder diffraction patterns calculated from known crystal structures, existing algorithms should perform extremely well. Coehlo (2004) evaluated the SVD-Index algorithm on randomly generated triclinic unit cells and consistently recover the correct triclinic answer. How well existing algorithms can index unit cells calculated from known structures has not been established, it is likely very high.

For cubic lattice systems, the single free lattice parameter, a can be found rather simply by pencil and paper, each peak occurs at an integer value divided by a^2 . For tetragonal, hexagonal, and rhombohedral with two free lattice parameters, solutions can be reliably found without computation aids through graphical methods (Hull & Davey, 1921). The difficulty begins with orthorhombic cases of three free lattice parameters, however, computational methods reliably identify the correct unit cell (CITE). Monoclinic and triclinic lattice systems are known to be difficult for computational algorithms.

The direct prediction of unit cells by inversion of Eq. 16, given perfect data is hindered by several challenges:

1. It is underdetermined, there will always be more unknowns than equations.
2. It is fundamentally discrete.
3. There is missing data.
4. The unit cell representation is ambiguous and not unique.

The inverse problem posed by Eq. 16 is underdetermined, there are more unknowns than knowns. The powder diffraction indexing problem usually starts with a set of 20 observed peak positions $\{q_{obs}\}_{hkl}$. The lattice system equations relate each peak in the set to the same six lattice parameters. The relationships in Eq. 1 - 7 are relatively simple, and as shown in Eq. 1, can be formulated as a set of linear equations. However, each of the 20 equations is parameterized by a unique set of Miller indices $\{hkl\}$. If n_k peaks are chosen, there will be between $3n_k + 1$ and $3n_k + 6$ unknown parameters, there will always be three times more unknown parameters than equations. This is an under-determined inverse problem - more parameters being predicted than constraints that can be imposed. Determining the unknown parameters h , k , & l has long been recognized as the primary obstacle to powder diffraction indexing (de Wolff, 1961; de Wolff, 1968).

Eq. 1-7 shows the parameters being predicted are a mix of continuous and discrete values. The discreteness of the Miller indices adds additional challenges. Most advanced numerical methods struggle with discrete values. Further, our analysis treats Miller indices as sets of three integers, making them categorically discrete values with nominal labels without an easily defined relations between them.

The "unit cell" in these relations is an arbitrary mathematical representation of the repeating unit within a crystal as defined by convention. The IUCR defines the conventional unit cell as the smallest volume unit cell with a right-hand basis and edges along the lattice's symmetry directions. This is ambiguous, and there are multiple "settings" that describe the same unit cell. For example, the orthorhombic unit cell can be placed with any permutation of the unit cell lattices. In the monoclinic lattice system, convention dictates that the unit cell be so the monoclinic angle is β and it is obtuse. The monoclinic unit cell can be defined just as well with the monoclinic angle at α or γ and as an acute angle. Additionally, there are transformations beyond these simple permutations that convert C (base) and I (body) centered lattices or to move a glide plane from along a lattice vector to a diagonal.

There are additional ambiguities when considering the centered Bravais lattices which exist for all lattice systems except triclinic. In these cases, the minimum volume unit cell that describes the crystal's repetition is a triclinic (OR XXX???) lattice system. However, a larger volume unit cell also describes the crystal at a higher degree of symmetry, lending easier mathematical analysis. Convention dictates the use of the centered Bravais lattices

There are other definitions that seek to remove this ambiguity, such as the reduced unit cell (Buerger 1957, CITE SELLING REDUCTION), or the s_6 (CITE) and g_6 spaces (Andrews & Bernstein 1988). These definitions are still retain ambiguities (Andrews 2019).

Unit cells are not generally unique. There are special cases where multiple, conventional unit cells can produce the same diffraction peak spacings. These unique cells are not simply different settings or representations of the same unit cell, but completely different unit cells. These cases have been tabulated, allowing their resolution (Oishi-Tomiyasu, 2016).

1.3 Overview of existing powder diffraction indexing algorithms

Shirley (2003) gives a good overview of the history of powder diffraction indexing.

1.3.1 Dichotomy method

ADD DISCUSSION ON DICVOL.

1.3.2 Zone Indexing

The zone indexing method, first described by Runge (1917), rediscovered by Ito (1949), refined by de Wolff (1957, 1958), and implemented computationally by Visser (1969) demonstrates a methodological approach to determining the angles of a triclinic lattice. For the monoclinic case, the method starts with the assumption that the reciprocal lattice vectors a^* and ca^* have been determined by the position of the low angle reflections. If the monoclinic angle, β^* is 90° , there will be a diffraction peak at $q_{h0l}^2 = h^2a^{*2} + l^2c^{*2}$. When the monoclinic angle is not 90° , this peak will be split, with two peaks occurring at $q_{h0l}^2 = h^2a^{*2} + l^2c^{*2} + 2hla^*c^*\cos(\beta^*)$ and $q_{h0-l}^2 = h^2a^{*2} + l^2c^{*2} - 2hla^*c^*\cos(\beta^*)$. The monoclinic angle is obtained from difference of these two peaks, $\cos(\beta^*) = \frac{q_{h0l}^2 - q_{h0-l}^2}{4hla^*c^*}$.

This method demonstrates the difficulty in determining lattice angles from powder diffraction. First, an assumption is made that the lattice parameter lengths have been accurately determined. Then, a both sides of the split peak must be observed and identified. Lastly, the angle is determined from a combination of two peak positions and two lattice parameters. In practice, this is performed through a guess and check method and requires powder diffraction patterns determined at high accuracy.

This method should struggle with poor data. Missing low angle peaks will preclude lattice parameter determination. Contaminant peaks will add confusion to lattice parameter determination and identification of peak pairs. Error in peak positions will compound to a larger error in angle.

Machine learning methods for unit cell determination have not been demonstrated to determine unit cell lengths to the precision necessary to use in the zone indexing algorithm.

1.3.3 SVD-Index

The method presented here draws inspiration heavily from the SVD-Index indexing presented by Coehlo (2003). This algorithm takes a generate-and-test approach to the problem, it starts with random guesses of the lattice parameters, then iteratively assigns Miller indices and optimizes the lattice parameters to explain the observed diffraction spacing's. This is a complex algorithm and an abridged overview is given here to support the development of ML-Index. SVD-Index consists of three primary components: 1) Initial unit cell generation; 2) Miller index assignment; and 3) Unit cell optimization.

SVD-Index generates initial unit cell candidates by randomly generating numbers for the unit cell parameters, then rescaling the parameters to match a given unit cell volume. The algorithm incrementally increases the unit cell volume that is used for rescaling until a solution is found. This is a brute-force grid search of the entire parameter space. While inefficient, SVD-Index compensates with speed. Candidate entries are rapidly tested, with nearly 100,000 candidates tested in a matter of seconds. This is a very powerful approach, no assumptions are made regarding how the input diffraction maps onto unit cell parameters. These assumptions could easily lead to algorithm omitting the neighborhood of the true unit cell parameters from the search space in the presence of contaminate diffraction or heavily missing peaks, causing it to fail to find the correct unit cell parameters.

Miller index assignment starts by establishing a reference set of Miller indices. This is done by calculating all possible Miller indices up to a certain resolution cutoff given by the unit cell volume. For each reference Miller index and candidate unit cell, the forward models (Eq. 1-7), are used to calculate reference peak spacings, $\{q_{ref}\}_{hkl}$. Observed peaks are assigned the Miller index associated with the closest reference peak.

Unit cell parameters are optimized to match the agreement between the observed, $\{q_{obs}\}_{hkl}$, and calculated $\{q_{cal}\}_{hkl}$ peak spacings. This is performed using weighted least squares solved by singular value decomposition (SVD). The forward models (Eq. 1-7) are formulated as a linear function of Miller indices, H , and a transformation of the unit cell parameters, \vec{x} , $\vec{q}_{cal} = H\vec{x}$. The least squares solution to \vec{x} to $w_{hkl}\vec{q}_{obs} = w_{hkl}H\vec{x}$, where w is a set of weights for each peak, is then found using SVD (CITE). The weight function is

$$w_{hkl} = d_{obs,hkl}^m |2\theta_{obs,hkl} - 2\theta_{cal,hkl}| I_{obs}. \quad (18)$$

Here, $d_{obs,hkl}$ and $2\theta_{obs,hkl}$ are the observed peak spacings in resolution (d-spacing: $d = 1/q$) and angular units. $2\theta_{cal,hkl}$ is the calculated peak spacing in angular units. I_{obs} are the peak's integrated intensity. The ideal exponent, m , was noted to be 4, however using a random number generated between 0 and 4 was found

to be the superior choice. This randomness is important to note, it is suggestive that a greedy algorithm, one that always picks the most probable next step, will not be able to find the correct unit cells.

This algorithm works by assuming a lattice system, and exhaustively searching for a solution within each lattice system.

1.4 Data-driven indexing approach

ML-Index is built within the SVD-Index framework and seeks improvements in 1) initial unit cell candidate generation, 2) candidate optimization, 3) identification of the correct unit cell from optimized candidates. It is developed using a large volume of synthetic data calculated from database entries.

For initial unit cell candidate generation, data-driven models are developed that generate unit cell candidates given a peak list input. For ideal unit cell generation, a model must be robust, it must produce some predictions reasonably close to the correct solution. Ideally it would be efficient, a significant fraction of candidates are generated in this neighborhood. We have not found that any model is particularly robust. To increase robustness, a collection of weak models is developed that function in different ways.

These include random forest models where unit cells are sampled from individual decision trees. A neural network model that predicts a mean and variance of the unit cell parameters, unit cells are generated by sampling from a Normal distribution with this parameterization. For each Bravais lattice, an ensemble of these two models are trained on data grouped by unresolvable unit cell ambiguities or expected differences in peak spacing "distributions" caused by different patterns of systematic absences.

A "Miller index template" model, in a manner similar to TREOR (Make sure this is a good comparison and cite), however done at a larger scale. For each Bravais lattice, thousands of random sets of Miller indices are generated based on the observed distribution of Miller indices in a training set. Given a set of observed peak spacings, unit cells can be determined for each template using least-squares methods.

A random unit cell model is developed where a random forest model is used to predict unit cell volume. Then unit cells are randomly generated and scaled so the unit cell volume matches the volume from a randomly sampled prediction from a decision tree. For each bravais lattice, one Miller index template and random unit cell model is developed.

For candidate optimization, we take the iterative optimization approach developed in SVD-Index. This optimization attempts to invert a mixed integer linear model. These models are most successfully solved using mixed integer linear programing algorithms (MILP). SVD-Index is an implementation of MILP algorithm designed specifically for powder diffraction indexing.

Identification of the correct unit cell from the list of optimized candidates is done with by de Wolff's figure of merit, the M20 score.

2 Methods

2.1 Data

Crystallographic data for training the machine learning models are sourced from the Cambridge Structural Database (CSD) and the Crystallographic Open Database (COD). These databases do not contain experimental data, they contain structural information about materials that were determined experimentally. Powder diffraction patterns are calculated from entries in these databases. This synthetic data is split into training and validation sets. The generative unit cell models are trained with the training data and validated with the validation data. The unit cell optimization procedure is developed exclusively using the validation data. Neither the training or validation sets are proper indicators of algorithm performance. The model development is biased towards their solutions and they lack "character" of real data. After development, real experimental data is used for a final evaluation. We employ three sources of experimental data. First is our internal data from smSFX experiments. Second is powder diffraction data sourced from tutorials. Third are powder diffraction patterns from the RRUFF database (Lafuente, et. al., 2015).

2.1.1 Preparation

The first step of the dataset generation process is an initial quality control of entries in the CSD and COD. The following criteria must be met by an entry for its inclusion in either training or validating the machine learning models.

1. Chemical formula must be listed.

2. Spacegroup number must be listed and between 1 and 230, inclusively.
3. The Hermann–Mauguin symbol must be obtainable from the listed spacegroup symbol.
4. The lattice system must be listed and compatible with the given conventional unit cell parameters.
5. A Niggli reduction, conversion from the conventional to reduced setting, must be successful.
6. Unit cell volume calculated from the given conventional and reduced unit cell parameters must match the given volume.
7. Unit cell volume must be consistent with the number of atoms in the unit cell deduced from the chemical formula. The given volume in Å³ must be within an order of magnitude of 18 times the number of atoms in the unit cell (CITE).

The next step is a duplicate removal step performed on the CSD and COD independently. A duplicate is defined as the following:

1. Belongs to the same Bravais lattice and,
2. The unit cell has the same chemical composition deduced from the chemical formula & the unit cell volume is within 5%.
3. or, The unit cell volume is exactly the same.

In the case of duplicate entries, the entry with the lowest reported r-factor is chosen. Databases are merged by first taking all the unique entries from the CSD, then only adding entries from the COD if they are not duplicated with an existing CSD entry. For the chemical composition of the unit cell, hydrogen and deuterium atoms, and atoms that comprise less than 5% of the total number of atoms in the unit cell are not taken into consideration. Many studies test the effects of changing one atom in a material. These entries could have nearly the same unit cell and very similar diffraction patterns. Omitting atoms that make up a small portion of the total number of atoms in the unit cell should consider these entries as duplicates.

I get the best performance for unit cell prediction when I use wide shallow neural networks, this was also observed by Vanessa. My understanding of wide shallow neural networks is they tend to work more by memorization as opposed to generalization. A strict duplication removal procedure could prevent the models memorizing identical patterns as opposed to generalization.

| Bravais Lattice | Total entries | Unique entries | Total entries | Unique entries | COD entries not in CSD |
|-----------------|---------------|----------------|---------------|----------------|------------------------|
| | CSD | CSD | COD | COD | |
| aP | 317,251 | 164,254 | 121,422 | 76,449 | 7,284 |
| cF | 1,171 | 870 | 9,236 | 3,343 | 3,121 |
| cI | 1,477 | 1,005 | 2,783 | 1,505 | 1,218 |
| cP | 2,859 | 2,074 | 4,437 | 2,687 | 2,090 |
| hP | 13,839 | 9,961 | 13,912 | 9,549 | 6,208 |
| hR | 12,749 | 8,601 | 8,768 | 5,892 | 3,192 |
| mC | 127,726 | 79,610 | 54,344 | 39,016 | 7,135 |
| mP | 493,166 | 207,248 | 183,224 | 97,372 | 9,425 |
| oC | 8,998 | 7,080 | 6,131 | 4,761 | 2,390 |
| oF | 4,658 | 3,708 | 2,021 | 1,718 | 386 |
| oI | 2,587 | 2,016 | 2,094 | 1,623 | 934 |
| oP | 186,790 | 87,848 | 72,705 | 43,483 | 7,854 |
| tI | 9,856 | 7,503 | 8,244 | 6,030 | 3,488 |
| tP | 15,388 | 11,204 | 9,841 | 7,010 | 3,112 |

Table 2: Duplicate entries in the CSD & COD

Datasets are generated from the unique database entries. The following information is extracted from each entry:

- Database source
- Identifier (If from CSD)
- Local cif file name (If from COD)

- Spacegroup number
- Bravais Lattice
- Lattice system
- Hermann–Mauguin spacegroup symbol
- Unit cell parameters
- Unit cell volume
- Peak lists

Two representations of the unit cell are included. First is the unit cell is taken directly from the the database. Second is a reindexed unit cell. Each entry is reindexed to a common setting for all entries with the same Bravais lattice, in an attempt to reduce ambiguities.

For the cubic, tetragonal, and hexagonal lattice systems, no reindexing is performed because there is no ambiguities in the unit cell representations.

For the rhombohedral lattice system, unit cells can be either placed in either a rhombohedral or hexagonal setting and frequently are listed in databases in the hexagonal settings. All entries are reindexed the rhombohedral setting.

For the orthorhombic lattice system, primitive (oP), face-centered (oF), and body-centered (oI) entries are reindexed so the unit cell lengths, a , b , c are in increasing lengths. Base-centered (oC) entries are placed in the C-centered (as opposed to A or B centered) setting such that cell length $a < b$. The base-centered entries could be placed in a setting such that unit cell lengths increase, however no common set of systematic absences will exist for these entries. Placing these entries all in the c-centered setting ensures the $h + k = 2n$ reflection condition must be met for all entries.

For monoclinic lattices, centered entries (mC) are conventionally placed in the base C-centered setting. For this work centered monoclinic entries are all placed in an equivalent body-centered setting. This allows further reindexing to enforce the lattice length a is shorter than c . For this reason as well, primitive entries (mP) with a glide plane, $P\ 1\ a\ 1$ for example, are reindexed so the glide plane is along the diagonal, $P\ 1\ n\ 1$.

Triclinic lattices are reindexed by applying a Selling reduction (Andrews 2019) and then choosing a reflection with increasing lattice lengths ($a < b < c$). The resulting unit cells have all obtuse angles.

Peak lists are created by identifying peaks in diffraction patterns. Diffraction patterns are calculated using the Computation Crystallography Tool box (CCTBX) with parameters based on internal datasets collected at SACLA in the fall of 2023 and spring of 2024. Each entry is loaded by a cif file and CCTBX is used to produce a peak list of all possible peaks between $2\theta = 1^\circ$ to 25° , at the wavelength of $\lambda = 0.827$ Å. This peak list contains the peak's integrated intensity, position in 2θ , and Miller indices. Intensities are scaled for the Lorentz-Polarization factor and peak positions are converted to units of $q^2 = 1/d^2 = \left[\frac{2\sin(\theta)}{\lambda}\right]^2$. A breadth is calculated for each peak using the formula $\beta = \beta_0 + \beta_1 q^2$. Peak breadths of experimental smSFX patterns were estimated and the parameterization of $\beta_0 = 0.00007$ and $\beta_1 = 0.002$ represents the average pattern. Three peak lists are created based on broadening of 2/3, 1, and 1.5 times this parameterization. Diffraction patterns are then created by summing gaussians with the amplitudes, locations, and standard deviations equal to the peak list's integrated intensities, peak position in q^2 , and breadths respectively. The summation axis occurs between $2\theta = 2^\circ$ to 25° in steps 0.01 2θ .

This diffraction pattern is divided by its total integrated intensity. Then peak positions are found using `scipy.signal.find_peaks` using a prominence=2 and distance=5. Prominence is the vertical distance between a peak and the lowest point between it and the next peak. Distance is the minimum horizontal distance between peaks with units of x-axis points. A distance of 5 would be equivalent to a separation of $2\theta = 0.05$. The peak positions found by `scipy.signal.find_peaks` will have positional error due to numerics and slightly overlapping peaks. To remove this error, the closest true peak to the found peak is select.

Figures 1-4 show examples of diffraction patterns and selected peaks. The blue curve is the powder diffraction pattern and the vertical lines are the peaks that were retained. The first 20 peaks are shown in a bolder dashed line and faint dotted lines are the later peaks.

2.1.2 Grouping

Ensembles of machine learning models are created by training multiple models on different groupings of data. These groupings are performed according to the hierarchy:

1. Lattice system, then

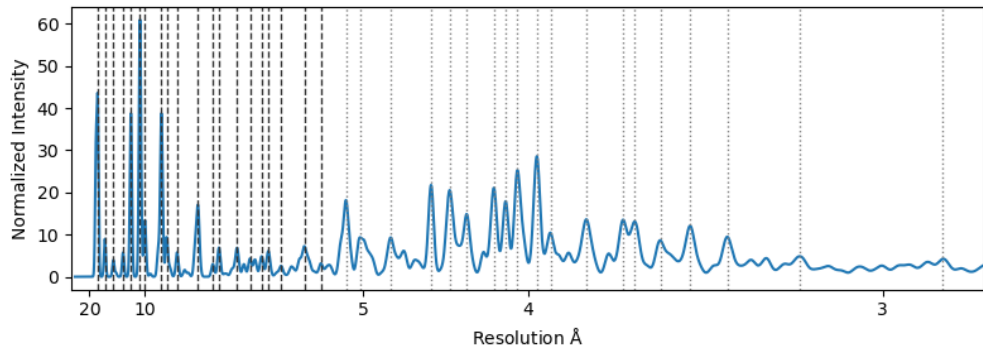


Figure 1: Example of the peak list generation from CSD entry BULCIW. This entry is monoclinic in the P 1 21/n 1 space group with unit cell parameters $a = 17.70$, $b = 20.02$, $c = 34.76$, $\beta = 98.459$

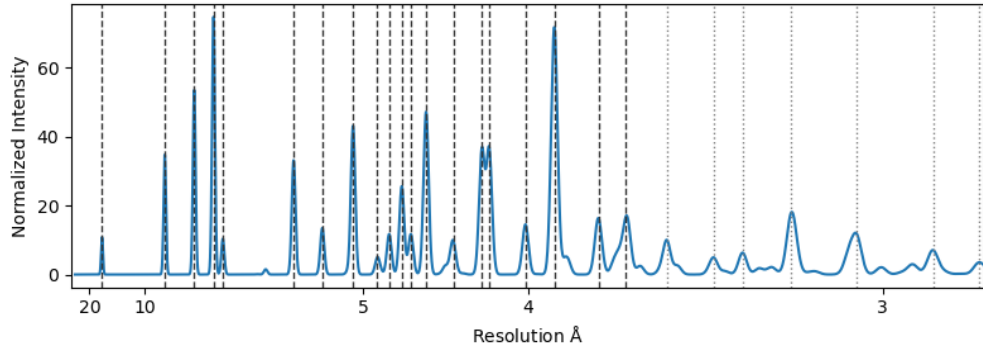


Figure 2: Example of the peak list generation from CSD entry BETDOW. This entry is monoclinic in the P 1 21/c 1 space group with unit cell parameters $a = 15.79$, $b = 10.7872$, $c = 9.8192$, $\beta = 102.512$

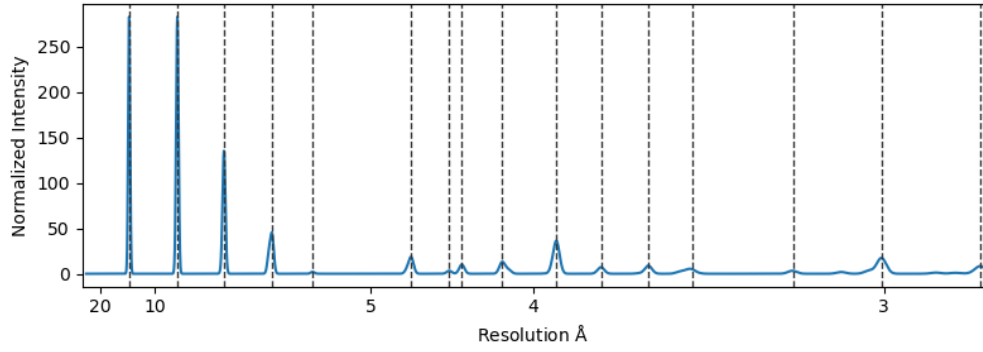


Figure 3: Example of the peak list generation from CSD entry BIDMUY. This entry is tetragonal in the I 41/a m d space group with unit cell parameters $a = 17.44$, $c = 17.74$

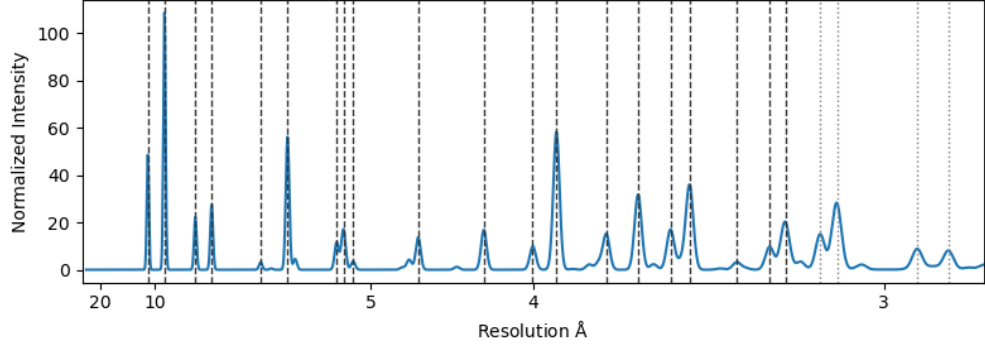


Figure 4: Example of the peak list generation from CSD entry AKEZOI. This entry is orthorhombic in the Pnma space group with unit cell parameters $a = 12.36$, $b = 21.01$, $c = 10.48$

2. Bravais lattice, then
3. Patterns in reflection conditions.

Grouping hierarchies 1 and 2 are well defined, and hierarchy 3 is subjective. This hierarchy is roughly based on the powder extinction class. In the original paper proposing using artificial neural networks to predict unit cell parameters (Habershon 2004), data was grouped into different powder extinction classes, and models were trained specifically for these groups.

To be clear what is meant by patterns in reflection conditions, consider the primitive orthorhombic space groups P 2 2 2 and P 21 21 21. P 2 2 2 has no systematic absences. The P 21 21 21 spacegroup has screw axis symmetry along the a , b , and c axes, leading to the reflection conditions that Miller index h must be even when $k = l = 0$; the $h00$ reflection must have an even h . The same condition is imposed on k and l for $0k0$ and $00l$ respectively. In the case that a mathematical model that determines the orthorhombic unit cell parameters, and does so by placing all of its emphasis on the low angle peaks which are more likely to have Miller indices 100, 010, and 001, It would first need to identify the difference between the P 2 2 2 and P 21 21 21 entries before predicting the unit cell parameters. If it cannot distinguish these cases, it should have great difficulty in predicting the unit cell parameters.

It should be noted that Hierarchy 3 splits up entries with the same space group. Consider spacegroup 18 which has two screw axes and one axis without a symmetry element. This one spacegroup contains spacegroup symbols P 21 21 2, P 21 2 21, and P 2 21 21. The P 21 21 2 spacegroup will have two reflection conditions $h00; h = 2n$ and $0k0; k = 2n$, and no reflection condition for l . The other two space symbols represent different permutations of the axes and reflection conditions. Again, orthorhombic crystals are reindexed so $a < b < c$, so all three settings will be contained in the training/testing datasets. Spacegroup 18 is split into three different groups, where they will be grouped with entries from other spacegroups with similar reflection conditions. On the other hand, consider spacegroup 17, with one screw axis and two axes without a symmetry element. This spacegroup contains symbols P 21 2 2, P 2 21 2, and P 2 2 21. Ideally, they would be split into different groups like Spacegroup 18, however, spacegroup 17, and other spacegroups with similar patterns in reflection conditions, have very few entries, so they are grouped into a single group due to limited data.

Specifications for the different groups can be found at "data/GroupSpec_lattice_system.xlsx" in the Github repository.

2.1.3 Training / Validation split

An 80 / 20% split is made for the training and validation sets. This split occurs at the level of the Hermann–Mauguin spacegroup symbol. So the separation of training and validation data is performed in groups of entries with common Hermann–Mauguin spacegroup symbol.

2.1.4 Parameter scaling

Neural networks perform best with inputs and outputs that are on the scale of one. So there is typically a rescaling of inputs and outputs so they look like a Normal distribution, or fit between 0 and 1. Training occurs considering each lattice system at a time. For a given lattice system, the observed peak spacing as \bar{q}_{obs}^2 , is scaled using a standard scaler. Meaning the mean and standard deviation of \bar{q}_{obs}^2 for all entries in the training set are calculated. Then the mean is subtracted from each peak spacing and the difference is divided by the standard

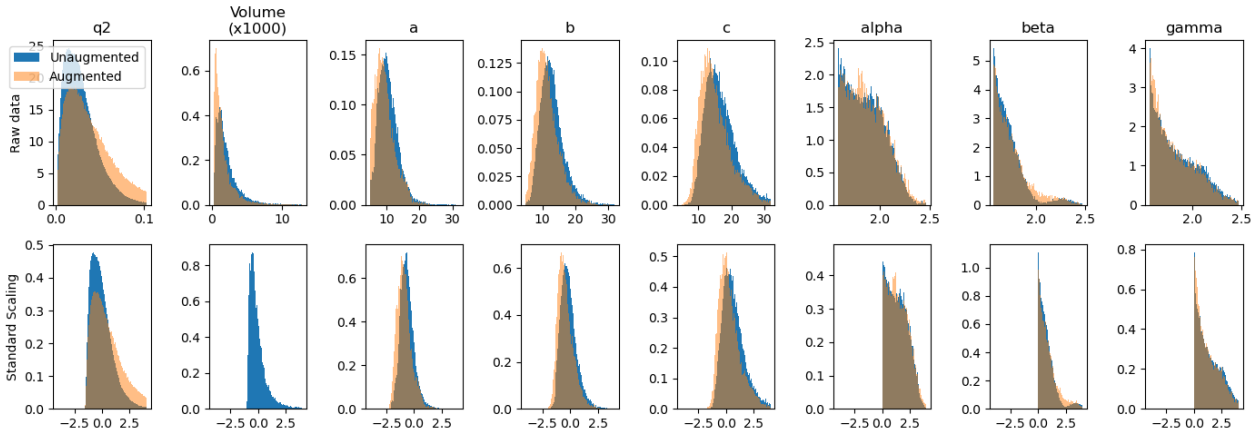


Figure 5: Data distributions for the triclinic lattice system. Top row plots the raw parameters for the unaugmented data in blue and augmented data in orange. The bottom row plots the parameters after scaling. The left column are the input peak spacings. The following columns are the unit cell parameters

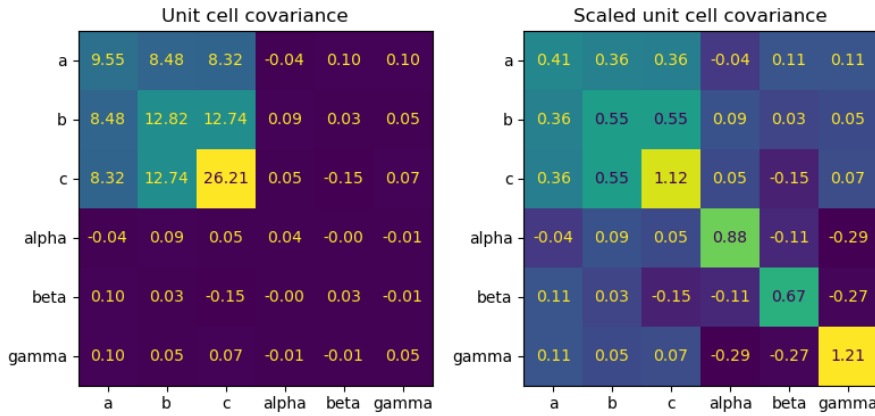


Figure 6: Covariance of the unit cell parameters for the triclinic lattice system. The left column is the covariance matrix for the raw unit cell parameters. The right column is the covariance after standard scaling has been applied.

deviation. All of the peaks are scaled with the same mean and standard deviation regardless of the order in the peak list.

Unit cell length parameters are also scaled using a standard scaler. For a given lattice system, the mean and standard deviation of all the unit cell lengths of the training set entries are calculated and used for scaling.

Unit cell angle parameters are converted to radians and subtracted by $\pi/2$. This puts right angles (90°) at zero. Then the standard deviation of all angles, which were not originally 90° , is calculated in radians, and the zero-centered unit cell angles are divided by this scale.

2.1.5 Reference Miller Indices

This work treats Miller indices as sets of three integers. These are categorically discrete variables that are assigned nominal labels based on the uniqueness of the peak position they would produce for any unit cell. Reference sets Miller indices are created for each Bravais lattice. First a large reference set with h , k , and l taking on all possible values from -40 to 40 is created. This list is first reduced to eliminate redundancy from lattice system constraints, to create a set of Miller indices that produce unique peak spacings for any unit cell of the given lattice system. These are given by the following formulas:

- Cubic lattice system

For each Miller index in the large reference array, $h^2 + k^2 + l^2$ is calculated. For each unique value of $h^2 + k^2 + l^2$, one set of Miller indices is retained. These are then sorted in order of increasing $h^2 + k^2 + l^2$.

- Tetragonal lattice system
 $h^2 + k^2$, and l^2 are calculated. For each unique set of $h^2 + k^2$ and l^2 , one set of Miller indices is retained. These are then sorted in order of increasing $h^2 + k^2 + l^2$.
- Hexagonal lattice system $h^2 + hk + k^2$, and l^2 are calculated. For each unique set of $h^2 + hk + k^2$, and l^2 , one set of Miller indices is retained. These are then sorted in order of increasing $\frac{4}{3}(h^2 + hk + k^2) + l^2$.
- Rhombohedral lattice system $h^2 + k^2 + l^2$ and $hk + kl + hl$ are calculated. For each unique set of $h^2 + k^2 + l^2$ and $hk + kl + hl$, one set of Miller indices is retained. These are then sorted in order of increasing $h^2 + k^2 + l^2$.
- Orthorhombic lattice system For each Miller index in the "all possible set", h^2 , k^2 , and l^2 are calculated. Each unique set of h^2 , k^2 , and l^2 results in a unique peak. These are then sorted in order of increasing $h^2 + k^2 + l^2$.
- Monoclinic lattice system h^2 , k^2 , l^2 , and hl are calculated. For each unique set of h^2 , k^2 , l^2 , and hl , one set of Miller indices is retained. These are then sorted in order of increasing $h^2 + k^2 + l^2$.
- Triclinic lattice system h^2 , k^2 , l^2 , hk , kl and hl are calculated. For each unique set of h^2 , k^2 , l^2 , hk , kl and hl , one set of Miller indices is retained. These are then sorted in order of increasing $h^2 + k^2 + l^2$.

These reference sets are further reduced by eliminate Miller indices that are systematically absent for the given Bravais lattice.

The last step to establish the reference set of Miller indices is a final sorting. The peak spacing is calculated for each of peak in the set of unaugmented training data given the reference Miller index. The average peak spacings are then averaged over all the entries. Then the reference Miller index set is sorted so these averaged peak spacings increase monotonically. Each reference set is then reduced to fixed length that differs from each set. Generally it is set so at least 99% of entries have all their observed Miller indices in their corresponding reference set. The Miller indices taken from the peak list are then assigned a nominal label corresponding to the position of the equivalent Miller index in the sorted reference list. If a peak's Miller index is not found in the reference list, which occurs because the equivalent Miller index is beyond the 100 or 500 length cutoff, it is assigned the last nominal label which is given a Miller index of (000).

2.1.6 Augmentation

The grouping approach requires a broad diversity of data, as opposed to just simply more data. A broader range of data allows for more groups. To increase the breadth of data, augmentation is performed, preferentially augmenting entries associated with Hermann–Mauguin spacegroup symbols with fewer entries. Augmentation happens after splitting the dataset into training and validation sets. If the original entry is in the training set, all entries augmented from this entry will remain in the training set and visa-versa for the validation set. A single entry is augmented at most 10 times.

Two augmentations need to be performed for each entry. First, the unit cell parameters are randomly perturbed. Second, the observed peaks are resampled from the non-systemically absent peaks. There are two implemented methods to randomly perturb the unit cell parameters, all of these perturbations occur in the scaled unit cell parameter space:

1. Random perturbation. A unit cell parameter for an entry is perturbed by randomly sampled from a Normal distribution with the original entry's unit cell parameter as a mean and 0.2 as the standard deviation. This perturbation occurs in the scaled unit cell space, so it is much larger than 0.2 Å.
2. SVD perturbations. An SVD is performed on the scaled unit cell parameters from the training set within a lattice system. The training set's unit cell parameters are then transformed into the new orthogonal basis from the SVD and the standard deviation of each component is calculated. An entry's unit cells are perturbed by transforming the scaled unit cell parameters using the SVD, then sampling new components from a Normal distribution centered at the entry's transformed component values and with a standard deviation equal to 0.2 times the standard deviation of that component calculated over the training set.

The random perturbation method is used only for the cubic lattice system because a SVD is not possible with one parameter. All lattice systems other than cubic use the SVD perturbation method. The SVD methods were implemented so any correlation between unit cell parameters observed in the training data would be retained in the augmented entries.

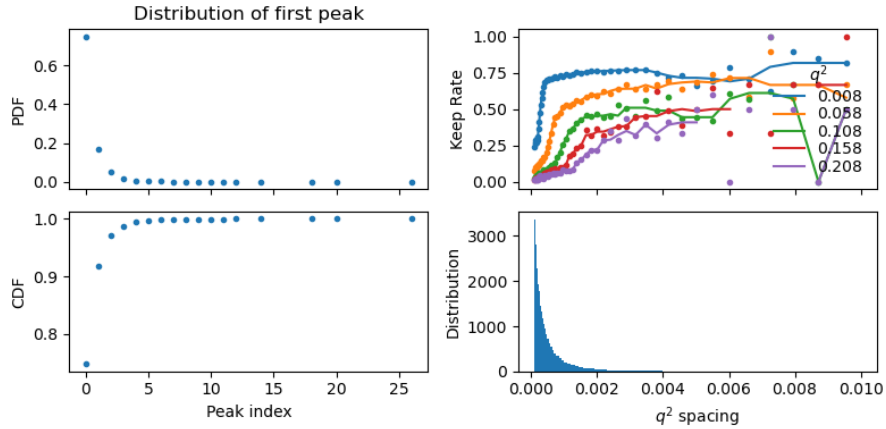


Figure 7: Augmentation statistics for the triclinic lattice system determined from the training entries. The left column is the probability distribution for the index of the first observed peak in the list of all non-systematically absent peaks. The top left plot is the PDF and bottom plot is the CDF. The lower right column plots the distribution of spacings between all possible non-systematically absent peaks. The upper right plot is the probability that a peak is observed vs. the separation from its closest neighboring peak. The different colors represent different ranges of absolute peak position. The markers are the observed data and the solid lines are the fit curves.

The peak list is augmented by resampling peaks from the list of non-systematically absent peaks. This resampling method was developed so the distribution of peaks in the augmented entries matched the distribution of the unaugmented entries. Generally, a peak is less likely to be observed at higher scattering angles and in close proximity to other peaks. Resampling picks peaks probabilistically based on an empirical distribution established from the training data.

There are two peak lists available at this time; Peak list 1, the first 60 non-systematically absent peaks. Peak list 2, the first 60 peaks that could be realistically observed in a diffraction pattern. The position of the first observed peak in the list of all non-systematically absent peaks is recorded. An empirical distribution is made from a histogram of this position list. Then the rate that subsequent peaks are observed is recorded as a function of q^2 and Δq^2 , the distance from the next closest non-systematically absent peak. This 2D grid of observation rates is then linearly interpolated using `scipy.interpolate.RegularGridInterpolator` to create the empirical distribution for acceptance probability, $\rho_{acc}(q^2, \Delta q^2)$.

The resampling algorithm proceeds by first selecting the first peak based on the distribution of first peak positions. Then, the list of non-systematically absent peaks is stepped through. There are three different cases for peaks, given it has a full width half max, β_{FWHM} , determined from the broadening equation used in peak generation. If two peaks are closer than β_{FWHM} , it is assumed they cannot be resolved as separate peaks.

1. Peak is within $\beta_{FWHM} / 1.5$ of the preceding selected peak. Reject peak.
2. Peak is further than $\beta_{FWHM} / 1.5$ of the preceding selected peak and the next peak in Peak list 1. Accept peak with probability $\rho_{acc}(q^2, \Delta q^2)$.
3. Peak is further than $\beta_{FWHM} / 1.5$ of the preceding selected peak and within $\beta_{FWHM} / 1.5$ of the next peak in Peak list 1. Accept peak with a probability of $0.5\rho_{acc}(q^2, \Delta q^2)$. This assumes that if two peaks overlap, at most one will be observed. Which peak is completely random. If the peak is accepted, the next will fall under case 1 and be rejected. If rejected, the next peak will fall under case 2.

The peak resampling method is a bit complicated. I arrived at it by trying to ensure the distribution of Miller indices in the augmented set matched the distribution in the unaugmented set.

2.2 Unit cell generator models

Unit cell generator models are developed to use their outputs to randomly generate unit cell candidates based on a set of peaks. For all lattice systems except cubic, 20 peaks from peak list 2 are used. For cubic lattice systems, 10 peaks are used because there tend to be fewer observable peaks in the diffraction patterns and 10 peaks are sufficient for one free parameter.

These models should be evaluated based on two criteria, robustness and efficiency. Given a neighborhood near the true unit cell parameters, robustness is the ability of a model to generate a minimum number of

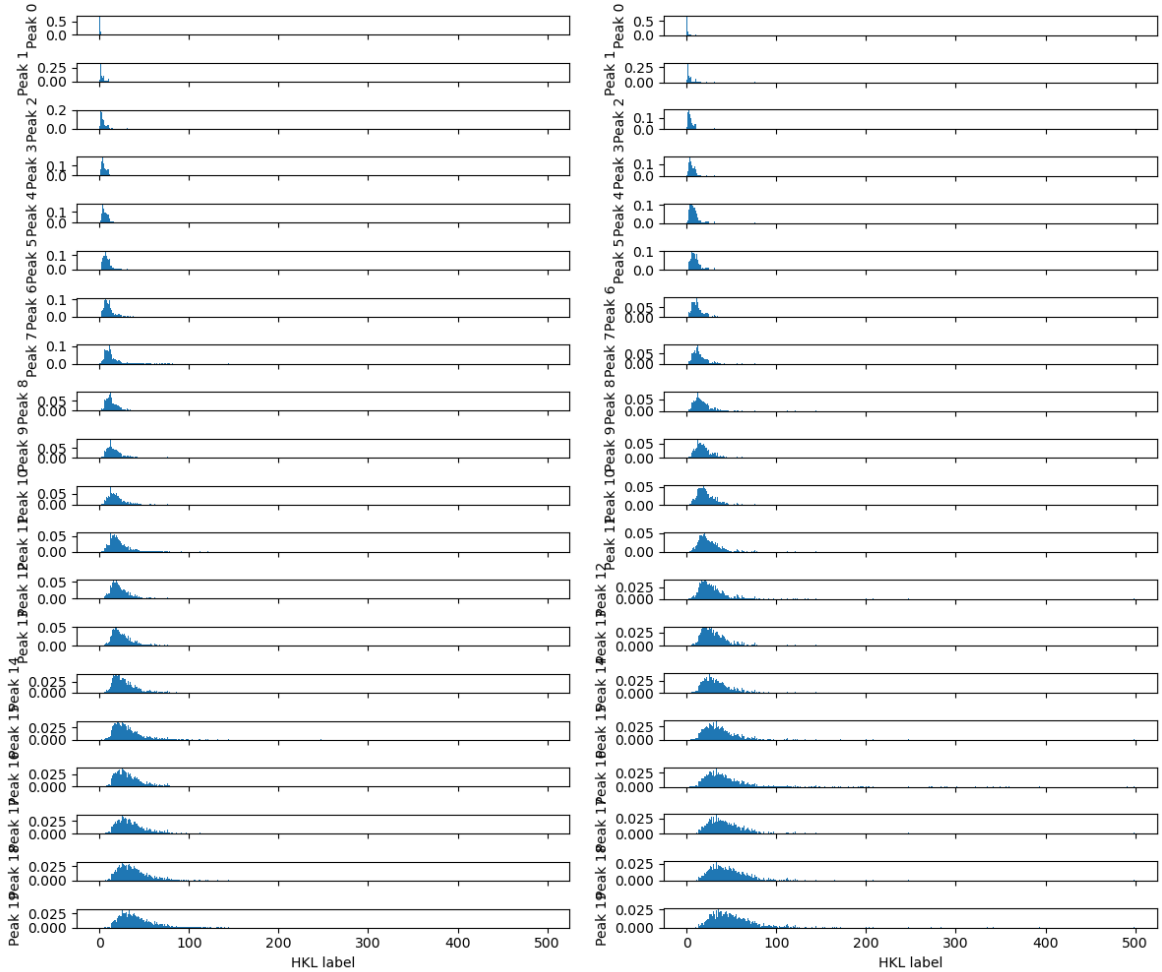


Figure 8: Unaugmented

Figure 9: Augmented

Figure 10: Distribution of nominal Miller set labels for triclinic. These can be used for diagnostics of the augmentation process. The distributions should look the same for the augmented and unaugmented entries.

candidate unit cells within the neighborhood and efficiency is the fraction of generated entries within the neighborhood. Robustness is the most important quality as candidates must be generated near the correct value in order for a solution to be found.

2.2.1 Neural Networks

Regression neural networks are set up as variance networks (Nix & Weigend, 1994). They output a mean and variance and are trained using a negative log-likelihood target function, which assumes a Normal likelihood. The approach presented here is based heavily on recent research on Variance networks (Detlefsen, et. al., 2019; Seitzer, et. al., 2022; Stirn & Knowles, 2021; Stirn et. al., 2022). Features implemented from this work include:

1. A distribution is predicted for variance as opposed to a point estimate. The Inverse-Gamma distribution is the posterior distribution for the unknown variance of a Normal distribution and is parameterized by α_{σ^2} and β_{σ^2} . The neural network outputs three values for each unit cell parameter, mean= μ , α_{σ^2} and β_{σ^2} .
2. Each model contains three parallel neural networks outputting μ , α_{σ^2} and β_{σ^2} separately. These networks start independently from the input peak spacings and have no connections with each other.
3. The training occurs cyclically. First, the weights of the μ network are optimized while the weights of the α_{σ^2} and β_{σ^2} networks are held fixed. Then the weights of the μ network are fixed while the weights of the α_{σ^2} and β_{σ^2} networks are optimized. Generally, each cycle is run for 10 epochs, and five cycles are performed.
4. A β -NLL target function is used when training the μ network and an NLL target function is used when training the α_{σ^2} and β_{σ^2} networks. The NLL target function is defined as:

$$L_{NLL} = \sum_{i=0}^{n_{uc}} \frac{1}{2} \ln(2\pi) - \alpha_{\sigma^2,i} \ln(\beta_{\sigma^2,i}) - \ln(\Gamma(\alpha_{\sigma^2,i} + 1/2)) + \ln(\Gamma(\alpha_{\sigma^2,i})) + (\alpha_{\sigma^2,i} + 1/2) \log(\beta_{\sigma^2,i} + \frac{1}{2}(uc_i - \hat{uc}_i)^2). \quad (19)$$

Here, the summation occurs over the unit cell parameters, uc_i are the true unit cell parameters, and \hat{uc}_i is the estimated mean. The β -NLL target function multiplies the NLL target function by the variance estimate raised to the power β_L . This multiplicative term is excluded from the gradients calculations, as denoted by the stop-gradient operator $\lfloor \cdot \rfloor$,

$$L_{\beta-NLL} = \sum_{i=0}^{n_{uc}} \left[\left(\frac{\beta_{\sigma^2,i}}{\alpha_{\sigma^2,i} - 1} \right)^{\beta_L} \right] \left[\frac{1}{2} \ln(2\pi) - \alpha_{\sigma^2,i} \ln(\beta_{\sigma^2,i}) - \ln(\Gamma(\alpha_{\sigma^2,i} + 1/2)) + \ln(\Gamma(\alpha_{\sigma^2,i})) + (\alpha_{\sigma^2,i} + 1/2) \log(\beta + \frac{1}{2}(uc_i - \hat{uc}_i)^2) \right]. \quad (20)$$

In the Inverse-Gamma distribution estimate of variance, the variance is estimated as $\frac{\beta_{\sigma^2}}{\alpha_{\sigma^2} - 1}$ where $\alpha_{\sigma^2} > 1$. The β -NLL target function raises this value to the power of $\beta_L = 1/2$ and multiplies the standard NLL target function.

I do not know which of the four of these points are important or not. There are still a few recommendations in the four papers referenced to improve the variance estimates that could be implemented.

There is an insidious memory leak in Tensorflow. I need to recompile the models between each cycle as the fixed weights and target function changes. Every time the model recompiles, a new "graph" is created in the backend of Tensorflow and the old graph is not released from memory. This is extremely bad when I am training 10 - 20 models per lattice system and I need to recompile the model 10 times during the training. I have spent some time trying to fix it without resolution. This is not the first time I have struggled with Tensorflow memory leaks and feel like jumping ship to Pytorch might be justified to solve this issue.

Each of the networks separately predicting μ , α_{σ^2} and β_{σ^2} are dense networks (MLP, Feed-forward). The default mean network uses three hidden layers of 200, 100, and 60 units. These hidden layers proceed in the following order, 1) Dense layer, 2) Layer Normalization, 3) GELU activation, 4) Dropout at a rate of 50%. The final layer is a Dense layer that outputs with linear activation.

The default α_{σ^2} and β_{σ^2} networks use two hidden layers of 100 and 60 units and are otherwise similar to the mean network. The final layer of the α_{σ^2} and β_{σ^2} networks uses a softplus activation to enforce a positive constraint on β and one is added to the α_{σ^2} network after softplus activation to enforce an $\alpha_{\sigma^2} > 1$ constraint.

All training occurs with the Adam optimizer using a learning rate of 0.0001 and a batch size of 64. The Neural networks are implemented in TensorFlow.

I have not done any hyperparameter optimization. There is a lot of over and underfitting.

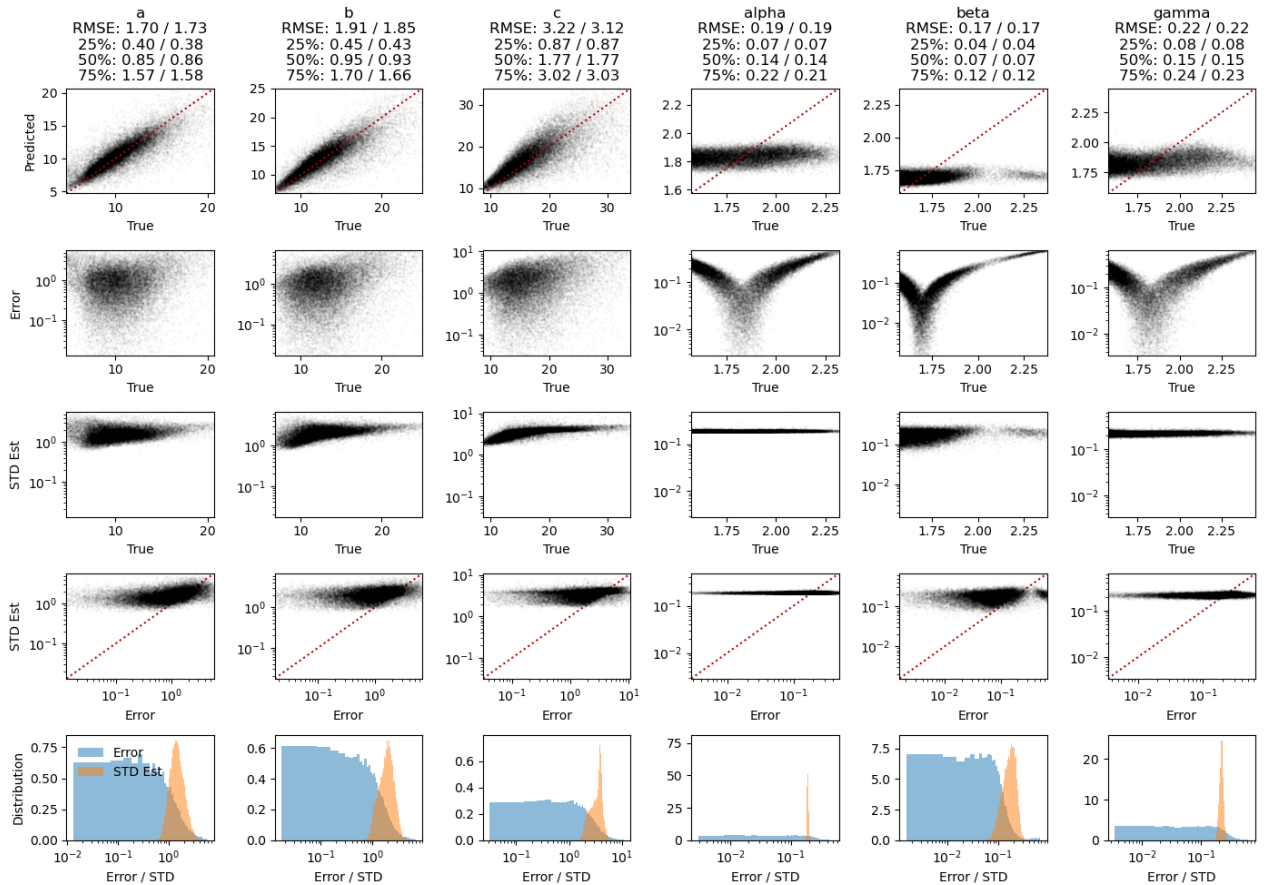


Figure 11: Regression results for the neural network model. The top row plots the predicted vs true unit cell parameters. The second row plots prediction error vs true parameters. The titles print the RMSD and percentiles for the training and validation sets.

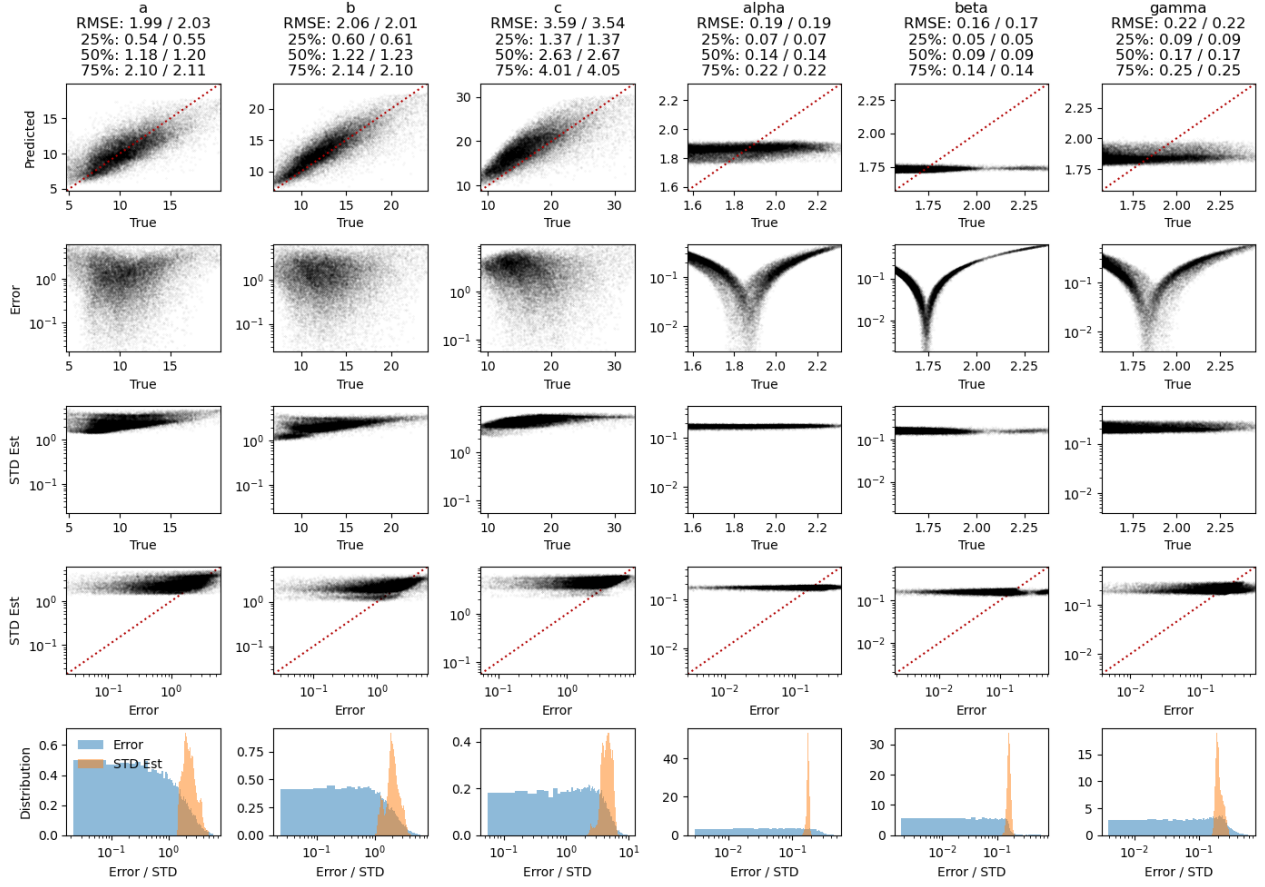


Figure 12: Regression results for the random forest model. The top row plots the predicted vs true unit cell parameters. The second row plots prediction error vs true parameters. The titles print the RMSD and percentiles for the training and validation sets.

2.2.2 Random Forest

In addition to the neural networks described in Section 2.2.2, random forest regression models are fit for each group of data. These are implemented using SKlearn with the parameters: 80 decision trees each trained with a 10% subsample of the training set and a minimum of 10 samples per leaf. Otherwise, the parameters were the defaults of `sklearn.ensemble.RandomForestRegressor`.

Some hyperparameter optimization was performed on the triclinic lattice system. The triclinic random forest model used 2,000 decision trees each trained with a 5% subsample and a minimum of 1 sample per leaf.

2.2.3 Miller Index Templates

This model for unit cell generation is based on randomly generating template sets of Miller indices that can be used to analytically determine unit cells given a set of observed peak spacings. The templates are generated based on the observed distribution of Miller indices in the training set. To ensure robustness, there must be a balancing to prevent over-representation of more common unit cells. This balancing is performed to balance "dominant zones".

A crystal with a dominant zone is typically defined as having one axis that is relatively shorter than the other two. Diffraction peaks that contain information about this shorter axis will occur at relatively larger diffraction angles. This has two distinct effects on the powder diffraction pattern that affect the presence and content information about the short axis. First, there are relatively few peaks in the diffraction pattern that contain information about the short axis, and specifically, these peaks will not occur at low diffraction angles. Secondly, for peaks that do contain information about the short axis in addition to the other axes, the Miller index corresponding to the short axis will be numerically smaller.

We use two metrics to quantify dominant zones that target these two effects separately. The first metric targets the lack of information about one axis in the diffraction pattern, the second targets the distribution of

Miller indices for the short axis. This distinction is important, because the lack of information about one axis could be caused by unbalanced systematic absences along each axis or by unlucky chance of randomly unobserved peaks, in addition to differences in diffraction angles caused by differences in lattice length. For example, we reindex all base-centered monoclinic entries to the body-centered setting. In the transformation that converts a conventional c-centered monoclinic to the body-centered setting, the lattice vectors are transformed via $\vec{a}' = \vec{c}$, $\vec{b}' = \vec{b}$, $\vec{c}' = -\vec{a} - \vec{c}$. Generally speaking, this should increase the magnitude of \vec{c} to \vec{a} . At first glance, this will increase the relative information about the c-axis making the "dominant zone" problem worse. However, the reflection conditions change from $h + k = 2n$ to $h + k + l = 2n$, introducing the $l = 2n$ condition when $(hkl) = (00l)$, which cancels out the first dominant zone effect of presence of information, but not necessarily the content of information effect.

The first metric is a new metric that quantifies the minimum amount of information about a single axis. For this metric, the number of peaks that contain information about each axis, the number of peaks with a non-zero Miller index, are calculated. Then the minimum of the three axes is taken. For each the three peak list $(001), (011), (111)$ contains one, two and three bits of information of information about axes a , b , and c respectively. This diffraction pattern would then be a one bit pattern.

The second metric is the ratio of the shortest to longest unit cell axis.

To start the Miller index template generation, the entries are separated into bins based on the information content (21 bins with values of 0 - 20 when there are 20 peaks). Within each bin, N templates are generated. If there are less than N entries in the bin, each entry is directly taken as a templating. Otherwise, templates are randomly generated based on the distribution of Miller indices in the training set. In this case, a histogram of the first peak's Miller set is taken as a probability distribution. The template's first Miller set is randomly sampled from this distribution. For the second peak, a histogram is created for the second peak's Miller set, given its first peak has the same Miller set as the random selection. The second Miller index is sampled from this distribution. This algorithm is repeated until each of the template's peaks are assigned or a histogram is attempted to be created from a single entry. In the latter case, the remaining entries Miller sets are used for the template's remaining peaks.

This procedure is then repeated based on binning on the second metric. Ten bins are created that span 0-1.

In the case that there are fewer than N entries in the bin, the ratio of N to the number of entries is recorded. Later, if a random subsampling of the peaks is performed, the ratios are normalized and used as sampling probabilities.

To generate a unit cell from the templates, first a random template is selected, then an optimization algorithm is performed to determine the unit cell:

1. Set $\vec{w} = 1/\vec{q}_{obs}^2$.
2. Solve a weighted version of Eq. 17, $\vec{w}\vec{q}_{obs}^2 = \vec{w}H\vec{x}_{nn}$. This is performed unit `numpy.linalg.lstsq` which solves the equation using the SVD method.
3. Calculate the forward model, $\vec{q}_{calc}^2 = H\vec{x}_{nn}$. If \vec{q}_{calc}^2 monotonically increases, accept \vec{x}_{nn} , otherwise,
4. Reorder the Miller index template to produce a sorted \vec{q}_{calc}^2 .
5. Set $\vec{w} = 1/\sqrt{\vec{q}_{obs}^2 |\vec{q}_{obs}^2 - \vec{q}_{calc}^2|}$.
6. Repeat starting at step 2 until a sorted \vec{q}_{calc}^2 is obtained or 10 iterations have been performed.
7. Record a loss $L = |1 - \vec{q}_{calc}^2/\vec{q}_{obs}^2|$.

After all the Miller index templates are generated, only unique templates are retained.

The loss is not currently used. Eventually I would like to use this as a metric to improve this process. The idea would be to view this templating method as a "feature extraction" layer. Combine metrics from the unit cell optimization and use as inputs to a random forest / neural network model that gives a sampling probability for the templates.

2.3 Optimization

The optimization process takes the generated candidates and iteratively optimizes them using the SVD-Index framework. The optimizer follows the steps:

1. Generation of candidates.
2. Redistribution of candidates.
3. Iterative optimization.
4. Postprocessing

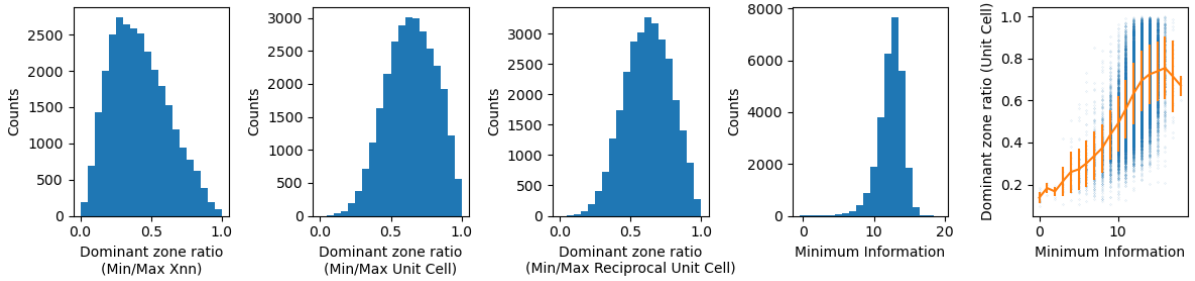


Figure 13: Dominant zone metrics for triclinic. The left three histograms are metrics for dominant zones based on unit cell values. These are quantified for the ratios of the x_{nn} parameters, the direct unit cell, and the reciprocal unit cell. The fourth plot is the minimum information. The rightmost plot is a scatter plot of dominant zone ratio vs minimum information. While these are correlated on average (orange line), there is considerable deviation from average.

2.3.1 Unit Cell Generation

Random unit cells are generated from the unit cell models.

| Model | Entries unable to place one close candidate | Efficiency |
|--------------------------------|---|------------|
| Neural Network | 306 | 2.28% |
| Random Forest | 206 | 2.52% |
| Templates | 87 | 2.57% |
| Neural Network & Random Forest | 137 | 2.39% |
| Neural Network & Templates | 72 | 2.42% |
| Random Forest & Templates | 54 | 2.54% |
| All | 49 | 2.45% |

Table 3: Evaluation of robustness and efficiency of random unit cell generators. For each unit cell generation model, 2,000 candidates were generated and the number of entries where the models failed to place one candidate within a 1 Å of the true unit cell is recorded as the middle column. The percentage of candidates within this region is in the right column. This evaluation was performed using roughly 5,000 triclinic entries

2.3.2 Redistribution

The purpose of the generative unit cell models is to randomly initialize the candidates in a manner more robust and efficient than a purely random generation. By design, the distribution of starting candidates will not be uniform across the space of possible unit cells. While this is desirable, excessively high densities of unit cells are not. A redistribution algorithm is used to move candidates from oversampled to undersampled regions. This algorithm is based on nearest neighbors. A candidate that has more than a specified number of neighbors within a given neighborhood is considered oversampled. The excess neighbors are moved within the neighborhoods of undersampled candidates.

This algorithm relies on a distance metric between candidates and two parameters, the size of a neighborhood and the maximum number of nearest neighbors. Distances are calculated by the Euclidean distance between unit cells in the \vec{x}_{nn} space. This space is chosen because it scales linearly with the data, \vec{q}_{obs}^2 . Each a different threshold for distance and maximum number of neighbors is chosen for each lattice system. The algorithm follows the steps:

1. Pairwise differences of all the \vec{x}_{nn} of each initial candidate are calculated and the number neighbors is calculated for each candidate. This is the number of other candidates within the neighborhood size.
2. The candidate with most neighbors is selected. Its neighboring candidates are randomly selected and removed such that the primary candidate will be left with the maximum number of nearest neighbors.
3. Candidates with less than the maximum number of nearest neighbors are randomly selected and additional candidates are randomly generated by perturbing these selected candidates.

This algorithm is repeated until no candidates have more than the maximum number of nearest neighbors.

2.3.3 Iterative Optimization

The iterative optimization process follows the general frame work of SVD-Index. The steps used in this algorithm are:

1. Assign Miller indices.
2. Randomly subsample peaks
3. Update \vec{x}_{nn} by least-squares minimization.
4. Calculate the de Wolff figure of merit, the M20 score.

Miller indices are assigned by calculating the peak positions of the reference Miller indices given the current unit cell, \vec{q}_{ref}^2 . An observed peak is assigned the Miller index its closest reference peak.

$$\vec{q}_{ref}^2 = H_{ref} \cdot \vec{x}_{nn}.$$

$$\rho(q_{obs,k}|H_{k,j}, \vec{c}) = \frac{1}{\sqrt{2\pi}\sigma_{q^2}} \exp\left(-\frac{1}{2} \frac{(q_{obs,k}^2 - q_{cal,kj}^2)^2}{\sigma_{q^2}^2}\right). \quad (21)$$

Eq. 1-7 are used to calculate $q_{cal,kj}^2$. The standard deviation parameter, σ_{q^2} , is defined like the weighting by SVD-Index,

$$\sigma_{q^2}^2 = q_{obs,k}^2 |q_{obs,k}^2 - q_{cal,kj}^2 + \epsilon_{q^2}|. \quad (22)$$

Notably, the σ_{q^2} presented here does not include the randomness in the same way as the weighting in SVD-Index. Randomness is important to the algorithm and is included by other means.

2.3.4 Randomized Optimization

The candidates are optimized using a random search procedure. The general approach is to iteratively assign Miller sets and update unit cells with randomization applied to the Miller set assignment. There are different randomization methods and the ideal method has not been determined.

No randomization The first approach to randomization is to not include it. This is included to explain the general approach.

1. Given the current unit cell estimate, calculate the pairwise difference array, Δ_{q^2} . For each peak position, assign the closest peak, $\text{argmin}(|\Delta_{q^2}|)$. For all of the Miller set assignment algorithms discussed here, assume that there is a mechanism that prevents the same Miller set to be assigned to multiple peaks.
2. Update the unit cells given the new Miller set assignments. This could be performed by solving the linear model of Eq. 17. Instead this is treated as a nonlinear least squares and the unit cells are updated with a single Gauss-Newton step calculated from the negative log likelihood, where the likelihood function is specified in Eqs. 30 & 31.

$$\vec{x}_{nn,t+1} = \vec{x}_{nn,t} + \mathcal{H}_t^{-1} \nabla \ln[\rho(\vec{q}_{obs}|H_t, \vec{x}_{nn,t})] \quad (23)$$

Here, \mathcal{H}_t^{-1} is the inverse Hessian of the negative log likelihood and ∇ is the gradient operator.

3. Recalculate the negative log-likelihood given the current unit cell and Miller set assignments.
4. Ensure that the unit cell is within a physically realistic range. If not fix the unit cell.
5. If the negative log-likelihood is below a specified threshold, it is determined to explain the observed diffraction and retained. The threshold value is based on the numerical value when $q_{cal}^2 \approx q_{obs}^2$

$$\begin{aligned} -\ln [\prod_{k=1}^{n_k} \rho(q_{obs,k}|H_j, \vec{c})] &= -\sum_{k=1}^{n_k} \ln \left[\frac{1}{\sqrt{2\pi}\sigma_{q^2}} \exp\left(-\frac{1}{2} \frac{(q_{obs,k}^2 - q_{cal,k}^2)^2}{\sigma_{q^2}^2}\right) \right], \\ &= -\sum_{k=1}^{n_k} \ln \left[\frac{1}{\sqrt{2\pi}\sigma_{q^2}} \right] + \ln \left[\exp\left(-\frac{1}{2} \frac{(q_{obs,k}^2 - q_{cal,k}^2)^2}{\sigma_{q^2}^2}\right) \right], \\ &= \sum_{k=1}^{n_k} \ln \left[\sqrt{2\pi}\sigma_{q^2} \right] + \frac{1}{2} \frac{(q_{obs,k}^2 - q_{cal,k}^2)^2}{\sigma_{q^2}^2}, \end{aligned}$$

Now given $\sigma_{q^2}^2 = q_{obs,k}^2 |q_{obs,k}^2 - q_{cal,k}^2 + \epsilon_{q^2}| \approx q_{obs,k}^2 \epsilon_{q^2}$ when $q_{cal,k}^2 \approx q_{obs,k}^2$, this likelihood simplifies to

$$= \sum_{k=1}^{n_k} \ln \left[\sqrt{2\pi q_{obs,k}^2 \epsilon_{q^2}} \right],$$

As implemented, the number $\epsilon_{q^2} = 10^{-10}$ is a small value used to prevent a division by zero error. When

Subsampling In the subsampling case, instead of using all 20 peaks, the optimization is performed using only 15 peaks. This is the currently implemented method.

Instead of purely random, subsampling can be based on assignment probabilities. Instead of assigning Miller sets based on the closest reference peak, the assignment neural network is applied to generate a probability distribution over Miller sets for each peak. The most probable peak is chosen and its softmax value is retained. Subsampling is performed by choosing the peaks to be retained with probabilities according to the assignment softmaxes. The softmaxes are normalized so their sum adds to one.

Resampling In the resampling case, all 20 peaks are used, however, the Miller sets are randomly assigned according to their softmaxes.

And of course, it is possible to combine the resampling and subsampling cases.

References

- [1] Andrews, L. C., & Bernstein, H. J. (1988) *Acta Cryst.* A44 1009-1018.
- [2] Andrews, L. C., Bernstein, H. J. & Sauter, N. K. (2019) *Acta Cryst.* A75, 593-599.
- [3] Andrews, L. C., Bernstein, H. J. & Sauter, N. K. (2019) *Acta Cryst.* A75, 115-120.
- [4] Bergmann, J., Le Bail, A., Shirley, R., Zlokazov, V. (2004) *Z. Kristallogr.* 219 783–790.
- [5] Buerger, M. J., (1957) *Zeitschrift für Kristallographie* 109, 42-60.
- [6] Coelho, A. A., (2003) *J. Appl. Cryst.* 36, 86-95.
- [7] Detlefsen, N. S., Jørgensen, M., Hauberg, S. (2019) 33rd Conference on Neural Information Processing Systems (NeurIPS 2019), Vancouver, Canada.
- [8] Habershon, S., Cheung, E. Y., Harris, K. D. M., and Johnston, R. L. (2004) *J. Phys. Chem. A.* 108, 711-716.
- [9] Hull, A. W. & Davey, W. P. (1921) *Phys. Rev.* 17, 549-570.
- [10] Ito, T. (1949) *Nature*, 164, 755-756.
- [11] Lafuente B, Downs R T, Yang H, Stone N (2015) The power of databases: the RRUFF project. In: Highlights in Mineralogical Crystallography, T Armbruster and R M Danisi, eds. Berlin, Germany, W. De Gruyter, pp 1-30
- [12] Nix, D. A., & Weigend, A. S., (1994) IEEE,
- [13] Oishi-Tomiyasu, R. (2016) *Acta Cryst.* A72, 73-80.
- [14] Rhodes, B., & Gutmann, M. (2022) Enhanced gradient-based MCMC in discrete spaces
- [15] Runge, C. V. (1917) *Phys. Z.* 18, 509-515.
- [16] Schriber, E. A. ... (2022) *Nature* 601, 360-365.
- [17] Seitzer, M., (2022) arXiv:2203.09168v2
- [18] Shirley, R. (2003) *IUCr Comput. Commiss. Newslett.* 2, 48–54.
- [19] Stirn, A., Knowles, D. A., (2021) arXiv:2006.04910v3
- [20] Stirn, A. et al (2022) arXiv:2212.09184v1
- [21] Visser, J. W. (1969) *J. Appl. Cryst.* 2, 89-95.
- [22] Wolff, P. M. DE, (1957) *Acta Cryst.* 10, 590-595.
- [23] Wolff, P. M. DE, (1958) *Acta Cryst.* 11, 664-665.
- [24] Wolff, P. M. DE, (1961) *Acta Cryst.* 14, 579-582.
- [25] Wolff, P. M. DE, (1968). *J. Appl. Cryst.* 1, 108-113.